npj Materials Degradation

https://doi.org/10.1038/s41529-026-00745-4

Article in Press

A comparative study on the corrosion resistance of Ti-6Al-4V produced via material extrusion and other additive manufacturing technologies

Received: 10 June 2025

Accepted: 18 January 2026

Cite this article as: Lorenzi, S., Nani, L., Persico, T. *et al.* A comparative study on the corrosion resistance of Ti-6Al-4V produced via material extrusion and other additive manufacturing technologies. *npj Mater Degrad* (2026). https://doi.org/10.1038/s41529-026-00745-4

Sergio Lorenzi, Lorenzo Nani, Tommaso Persico, Mariangela Lombardi, Fabrizio Sarasini, Claudia Sergi & Marina Cabrini

A comparative study on the corrosion resistance of Ti-6Al-4V produced via Material Extrusion and other additive manufacturing technologies

Sergio Lorenzi[a], Lorenzo Nani[a]*, Tommaso Persico[a], Mariangela Lombardi[b], Fabrizio Sarasini[c], Claudia Sergi[c], Marina Cabrini[a]

[a]Department of Engineering and Applied Sciences, University of Bergamo, Italy

[b]Department of Applied Science and Technology, Polytechnic University of Turin, Italy

[c]Department of Chemical Engineering Environment Materials, University of Rome La Sapienza, Italy

*corresponding author, *lorenzo.nani@unibg.it*, via Galvani, 2, Dalmine (BG) 24044, Italy

Abstract

This study investigated the influence of process-induced surface features, porosity, and microstructure on the corrosion behavior of Ti-6Al-4V alloys produced by different additive manufacturing (AM) technologies, including emerging sinter-based material extrusion (MEX), well-established electron beam melting (EBM) and laser powder bed fusion (LPBF), and wrought reference material. The investigated manufacturing routes produced sensibly different surfaces, porosity, and microstructures. Potentiodynamic and potentiostatic polarization tests in phosphate-buffered saline (PBS) revealed stable passivity and excellent corrosion performance for all AM alloys, both in the as-built and polished conditions. After polishing, modest variations were detected among manufacturing technologies, suggesting a possible deleterious effect of the intrinsic porosity once exposed to the environment. Immersion tests performed in neutral and acidified isotonic solutions highlighted the onset of selective corrosion phenomena between the α and β phases under deoxygenated acidic conditions, consistent with Volta potential measurements. Long-term immersion in acidified isotonic solution further confirmed the detrimental influence of porosity on the corrosion behavior of Ti-6Al-4V, especially for the MEX-produced alloy, where the presence of a macro-defect network promoted localized corrosion propagation.

Introduction

Titanium and Ti-alloys exhibit exceptional mechanical resistance to weight ratio and outstanding corrosion resistance, making them ideal for high-performance applications in challenging industries like aerospace and biomedical fields [1]. Furthermore, their excellent biocompatibility and relatively low Young modulus enable their effective use in permanent biomedical devices such as osteosynthesis implants, prostheses and dental implants [2], [3]. Ti-6Al-4V is the most widely used among Ti-alloys, representing approximately half of the titanium market share, and is currently available as feedstock for several additive manufacturing (AM) technologies [4]. This last feature is particularly relevant for biomedical applications, as AM offers significant advantages over conventional manufacturing processes, enabling the production of patient-specific implants with complex geometries, optimized surfaces for osseointegration and reduced material waste due to the obtaining of near-net-shape products. Moreover, the ability to create lattice or hollow structures allows for tuning the overall component stiffness, preventing harmful phenomena such as stress shielding in orthopedic implants [5].

Electron Beam Melting (EBM) and Laser Powder Bed Fusion (LPBF) were among the first additive manufacturing techniques developed for titanium and its alloys, offering excellent mechanical properties due to rapid solidification, good dimensional tolerances, limited porosity, and a surface finish that can promote osteointegration. EBM is particularly advantageous as it features higher surface roughness and does not require post-processing heat treatments to recover residual stresses and martensitic α' phase, while also offering greater productivity if compared to LPBF [6]. Although some differences exist between these two technologies, both are widely adopted by several manufacturers of prostheses and biomedical implants [7].

Recently, sinter-based additive manufacturing technologies, such as Material Extrusion (MEX), have been gaining increasing interest as they overcome some of the limitations of the aforementioned well-established AM techniques, especially from an economic perspective [8], [9]. This method is based on the deposition of a polymeric filament loaded with metal powders, processed using a printing system analogous to those commonly employed for thermoplastic materials. The printed components, referred to as green parts, undergo a debinding stage to remove the polymeric binder, obtaining metal powder agglomerates known as brown parts. These are subsequently subjected to high-temperature sintering to achieve metallurgical bonding of the particles and densification of the part [10]. This AM technology is characterized by significantly lower equipment costs, resulting in a lower cost of the final component, while maintaining geometric flexibility, high surface roughness favoring osteointegration, and near-net-shape capabilities [11]. Furthermore, MEX ensures effective contaminations control, as it does not require the reuse of feedstock powders, which are moreover embedded in the polymeric filament. Despite the advantages listed, MEX technology's main drawback is the introduction of characteristic macro-defects, which typically form a periodic and interconnected network and can compromise the final properties of the material [12], [13].

Regardless of the production process, Ti-6Al-4V is a highly corrosion-resistant alloy suitable for environments far more aggressive than the human body. Previous studies on this alloy manufactured via both conventional and AM techniques (EBM and LPBF) have demonstrated the establishment of stable passivity in simulated body fluids, resulting in extremely low corrosion rates [14], [15]. However, conditions within the human body can change significantly in the presence of specific processes, such as inflammatory responses in periprosthetic tissues, which can cause the access of oxidizing species like hydrogen peroxide (H_2O_2) or radicals [16]. In addition, specific exposure conditions like the presence of crevices or the synergistic action of mechanical abrasion and crevice (mechanically assisted crevice corrosion, MACC [17]) can create much more aggressive local environments, with strongly acidic pH values [18]. For these reasons, the corrosion mechanisms and rates can vary considerably if compared to the typical environmental conditions of the human body, and severe localized and/or selective corrosion phenomena can occur. In these conditions, even materials with intrinsically high corrosion resistance such as Ti-alloys will deteriorate rapidly, leading to possible prosthesis failure. Furthermore, enhanced ion release can potentially trigger significant immune responses in surrounding tissues and lead to long-term complications due to the continuous release and accumulation of alloying elements in the human body [19]. Consequently, analyzing corrosion behavior and degradation rate is particularly crucial, as certain alloying elements, even in limited concentrations, may have adverse effects on the patient health. For example, this is the case for aluminum in Ti-6Al-4V alloy, which is known to have potential neurodegenerative effects [20].

Therefore, the unique surfaces, porosity and microstructures introduced by AM processes require further investigation to fully understand their impact not only on the mechanical behavior, but also on corrosion performances [21]. Since MEX technique has been proposed in recent research works as a promising alternative for the manufacturing of prosthetic devices [22], [23], this study extends the assessment of these aspects to MEX-manufactured Ti-6Al-4V. The results were compared with the more extensively studied EBM and LPBF AM techniques, as well as the conventional wrought alloy. A particular focus was placed on the role of the aforementioned endogenous defects and their impact upon exposure to the environment.

Results and discussion

Materials characterization

The as-built surfaces of the MEX, EBM, and LPBF specimens, reconstructed using a confocal profilometer, are shown in Figure 1. The corresponding roughness parameters, calculated in compliance with ISO 25178 standard, are reported in Table 1.

All the additively-manufactured specimens exhibited external as-built (AB) surfaces with high surface roughness. The MEX-produced surfaces were characterized by high roughness in both the analyzed directions, but with significant topological differences between them (Figure 1a,b). Specifically, the vertical surfaces (Z), parallel to the building direction (BD), showed higher peak-to-peak asperity (Sz) mainly due to the waviness generated by the deposited filament layers. This waviness was lower for the horizontal surfaces (XY), orthogonal to the building direction, also due to the aspect ratio of the deposited filament cross-section. However, the developed interfacial area ratio (Sdr) values of XY and Z surfaces were almost comparable. This can be ascribed to the presence of emerging sintered particles on both the considered directions (detailed view in Figure 1b), which proved to be more influential in increasing the overall surface than the macro-texture generated by filament deposition. Nevertheless, the deposited filament was easily recognizable in both directions and showed a dominant effect on the surface waviness only.

EBM and LPBF specimens also exhibited relevant differences between XY and Z surfaces (Figure 1c,d and Figure 1e,f, respectively). As already known from previous studies on these technologies *[24]*, Z surfaces presented only mild waviness, caused by the layer-by-layer production with relatively thin layers (30÷60 µm). Concurrently, they also showed several partially-melted particles (detailed view in Figure 1d,f) that sensibly increased roughness, both in terms of Sa and Sz, and also the overall Sdr. This effect was especially pronounced in the case of EBM, which uses powders with larger particle sizes to counteract a potential electrical charging resulting from the interaction with the electron beam. Conversely, XY surfaces displayed an almost complete absence of partially melted particles and only slight waviness related to the welding tracks, which typically depends on process parameters such as the hatching distance and the electron beam/laser spot diameter. This resulted in EBM and LPBF-processed Ti-6Al-4V having more pronounced variations between XY and Z surfaces regarding the Sdr parameter (Table 1).

The high roughness of the AM specimens may be troublesome for certain applications, requiring further improvement of the surface finishing. However, in the case of biomedical components such as orthopedic or dental prostheses it can be a desirable effect, because the increase in surface density has been proved to promote the osteointegration of the implant with the surrounding bone tissue *[25], [26]*. Micrometer-scale roughness (Sa 1-5 µm) is usually obtained via chemical etching or sandblasting on conventional prostheses and is known to support osseointegration by enhancing bone retention, protein adsorption and osteoblastic activity *[27], [28]*. AM alloys exhibited substantially higher roughness, which can be detrimental as it can promote bacterial adhesion *[27]*. Nonetheless, studies on EBM-produced Ti-6Al-4V report satisfactory osseointegration *[29]*, and evidence indicates that amplitude-based roughness parameters alone cannot fully predict cell adhesion or implant success *[30]*. This highlights the need for specific investigations on MEX-produced Ti-6Al-4V, given its distinctive surface topology with high waviness and local roughness more similar to conventionally-manufactured prostheses.

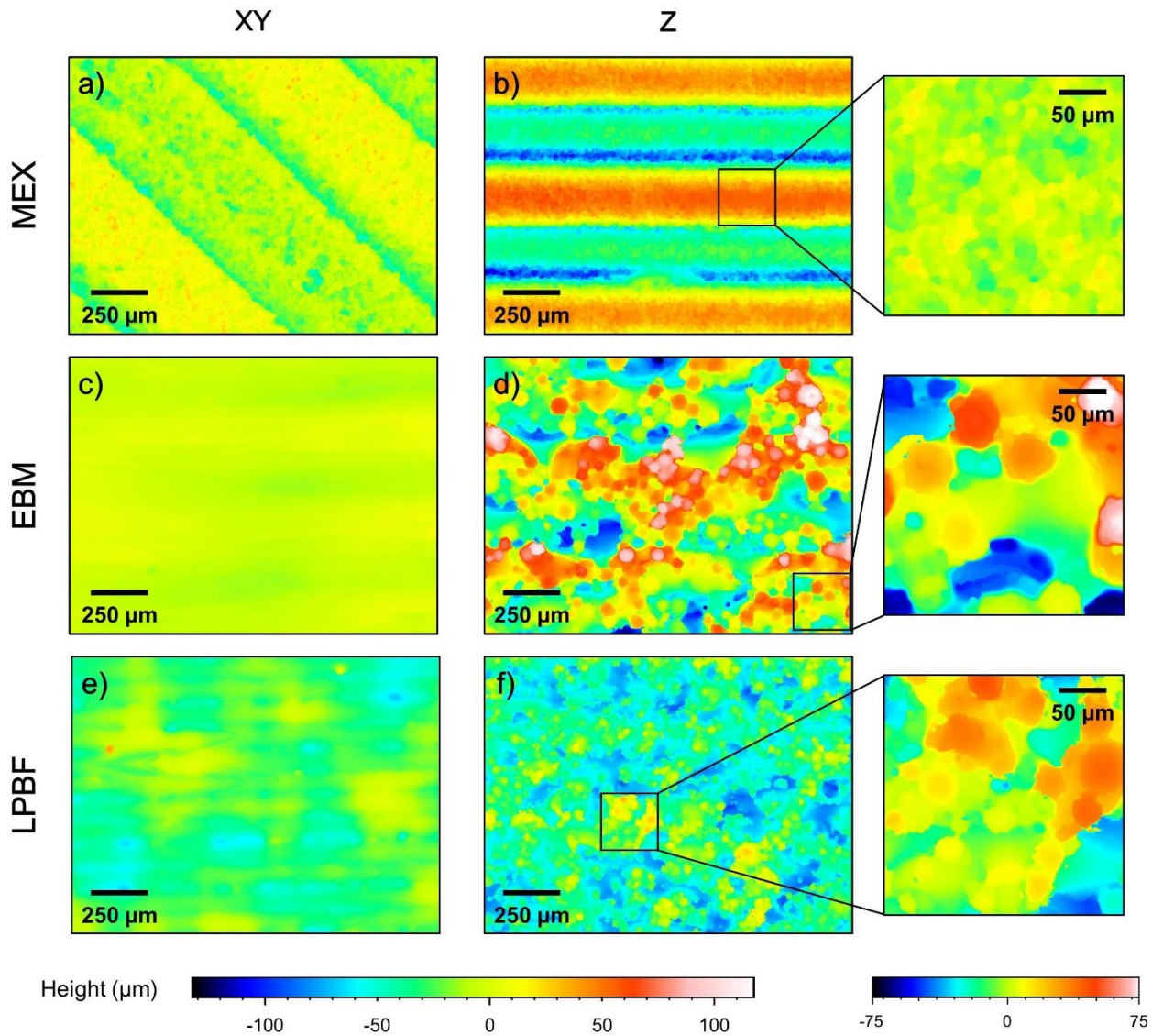

Figure 1 | Confocal surface reconstruction of the as-built AM specimens. Horizontal (XY) and vertical (Z) surfaces reconstruction of (**a,b**) material extrusion (MEX), (**c,d**) electron beam melting (EBM) and (**e,f**) laser powder bed fusion (LPBF) Ti-6Al-4V specimens, respectively. Local roughness, showed in the Z surface high-magnification images, was evaluated after applying a suitable form removal.

Table 1 | Roughness parameters calculated from the confocal surface reconstruction according to ISO 25178 (Sa= average surface roughness, Sz= peak-to-peak surface roughness, Sdr= developed interfacial area ratio).

	MEX		EBM		LPBF	
	XY	Z	XY	Z	XY	Z
Sa	11.3 µm	37.7 µm	4.4 µm	36.5 µm	7.1 µm	18.7 µm
Sz	84.1 µm	179.2 µm	34.8 µm	253.0 µm	83.5 µm	169.0 µm
Sdr	46.9 %	55.2 %	1.0 %	94.2 %	3.3 %	91.0 %

The cross-sectional micrographs at the optical microscope (OM) of the polished AM specimens are shown in Figure 2. The defects observed were found to be significantly different depending on the AM process adopted.

Ti-6Al-4V obtained through MEX showed linear and periodic macro-porosity on the cross section parallel to the build platform (Figure 2a), mimicking the deposition of the extruded metallic-polymeric filament. Furthermore, the inner core area, produced with a hatch angle of ±45°, and the peripheral contour area, with a filling pattern parallel to the outer edges, were clearly distinguishable. The alignment and repetition of the macro-defects was also observable on cross sections perpendicular to the build platform (Figure 2b) due to the layer-by-layer printing strategy. These results confirmed previous findings on other alloys obtained through MEX with the same deposition strategy (±45°), which furthermore highlighted that the porous network was interconnected in the core zone *[12], [13]*. Since macro voids are primarily associated with the deposition process, the porous network is governed by the deposition strategy adopted, including technological parameters such as filling pattern, nozzle diameter, hatch spacing, hatch angle and layer thickness. Furthermore, debinding and sintering parameters (time, temperature and atmosphere) and feedstock tuning are crucial to limit the formation of micropores, which were also present alongside macro defects. Such micropores are already known not only in MEX products, but also in materials processed by powder metallurgy or metal injection molding (MIM), of which MEX can be fully considered as an extension *[31], [32]*. Due to the above-mentioned micro and macro-porosity, the relative volumetric density of as built MEX components is typically sensibly lower than the EBM and LPBF counterparts, in the order of 90-97% *[33]*. Accordingly, image analysis measurements indicated a volumetric porosity of 6.6% in the MEX Ti-6Al-4V. This technology is still under improvement and several strategies are currently being developed both to reduce the overall porosity (e.g. via feedstock tuning or hot isostatic pressing, HIP) and/or to modify the morphology of structured macro-porosities, mitigating their effect on mechanical behavior *[12], [34], [35]*.

Otherwise, EBM and LPBF Ti-6Al-4V exhibited relatively small and mainly spherical porosities, homogeneously distributed in the materials (Figure 2c,d). Such defects can arise due to gas trapped inside the melt pool or also due to incorrect process parameters – mostly the volumetric energy density, VED – as in the case of keyhole collapsing pores or lack of fusion areas, alongside with cracks due to both incorrect process parameters or poor processability of the material *[36]*. However, with a careful tuning of the alloy-specific process parameters it is possible to obtain almost fully dense materials, with a relative volumetric density typically higher than 99% for both of these technologies *[37]*. Indeed, the EBM and LPBF Ti-6Al-4V under investigation exhibited 0.5% and 0.2% volumetric porosities, respectively.

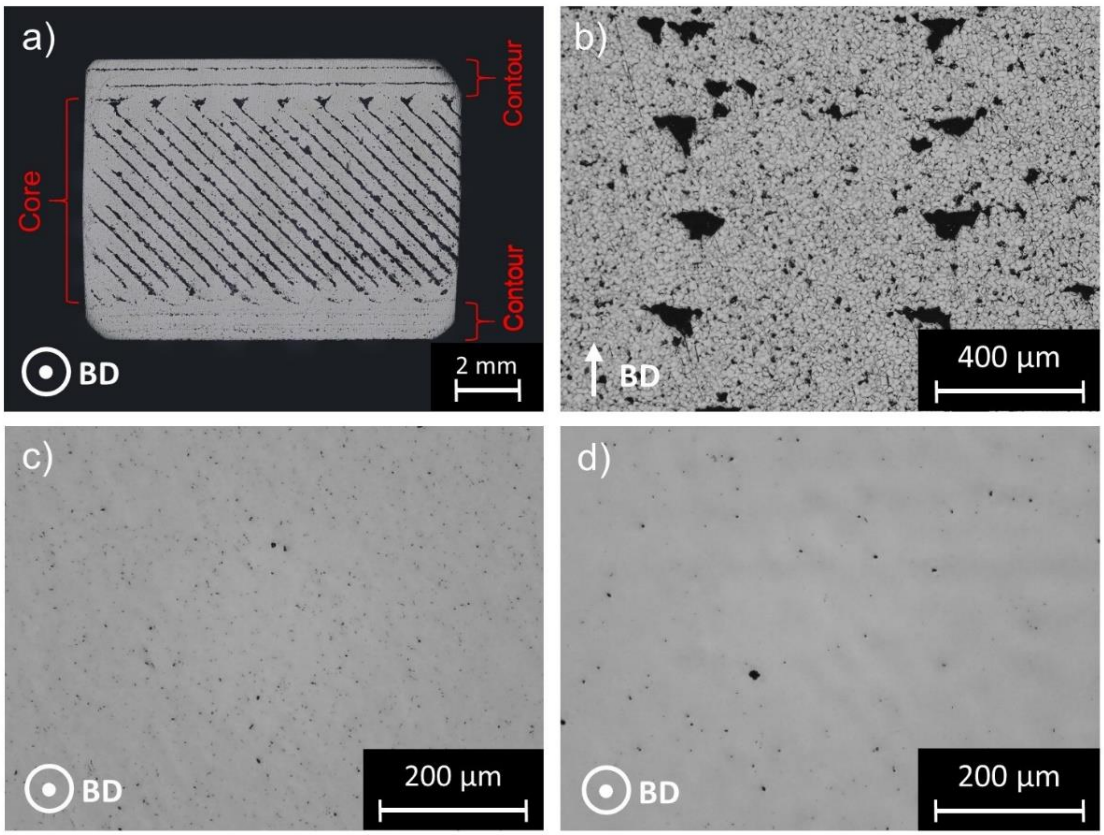

Figure 2 | Defects of the AM specimens. OM images of (a,b) MEX, (c) EBM and (d) LPBF Ti-6Al-4V polished specimens, highlighting the different voids morphologies; the macro-defects of MEX specimen clearly showed the core and contour regions and their respective hatch angles, as well as the porosities alignment along planes parallel to the build platform, due to the layer-by-layer deposition.

The specimens' microstructures were strongly influenced by the adopted manufacturing process, as illustrated by OM and field-emission scanning electron microscope (FESEM) micrographs reported in Figure 3. In fact, although the chemical compositions of the studied materials were comparable, and in all cases the typical α+β duplex microstructure was observed, the morphology and distribution of these phases changed considerably among different production technologies.

Indeed, MEX samples were characterized by equiaxed α-grain microstructure decorated with coarse regions of β-phase at the grain boundaries (Figure 3a,b), which formed an almost continuous network around the α-phase grains. This microstructure is typical for this alloy when sintered at a temperature within the α+β phase region, followed by slow cooling *[31]*.

On the other hand, specimens manufactured with powder bed fusion technologies (EBM and LPBF) exhibited a much finer microstructure, characterized by the presence of α-phase lamellae arranged in a Widmanstätten pattern, separated by fine β-phase regions (Figure 3c,d and Figure 3e,f, respectively). In addition, prior-β grains, characterized by a columnar morphology and aligned with the building direction, were clearly recognizable. These microstructural features are consistent with those reported in previous studies on Ti-6Al-4V alloy produced by EBM and LPBF *[38]*, *[39]*, *[40]*. The observed microstructures were a result of the high cooling rates of the molten bath in EBM and especially LPBF manufacturing processes (in the order of 10^4 K/s in EBM and 10^5-10^6 K/s in LPBF *[4]*, *[41]*). The α'-free microstructure

was obtained by means of post-process heat treatment in the case of LPBF, while with EBM the high building platform temperature (close to 700 °C) acted as an in-process heat treatment, which simultaneously reduced residual stresses and recovered the α' martensitic phase. The transformation of martensitic microstructure into a α+β duplex microstructure is of primary importance not only from a mechanical perspective, to mitigate material brittleness *[42]*, but also to enhance its corrosion resistance, as evidenced by the study of Cui et al., in which an improved corrosion resistance of LPBF-produced Ti-6Al-4V alloy was observed after annealing *[43]*.

The material obtained by conventional plastic deformation showed a microstructure characterized by α-grains of a much smaller size than those of MEX and with the presence of fragmented regions of β phase at the grain boundaries (Figure 3g,h). These results are referred to a cross-section perpendicular to the rolling direction, which is the same orientation that was analyzed with electrochemical and immersion corrosion tests.

In all the studied materials, energy dispersive spectroscopy (EDS) analyses highlighted higher contents of Al in the α phase and V in the β phase with respect to the average chemical composition, consistently with scientific literature *[44]*, *[45]*.

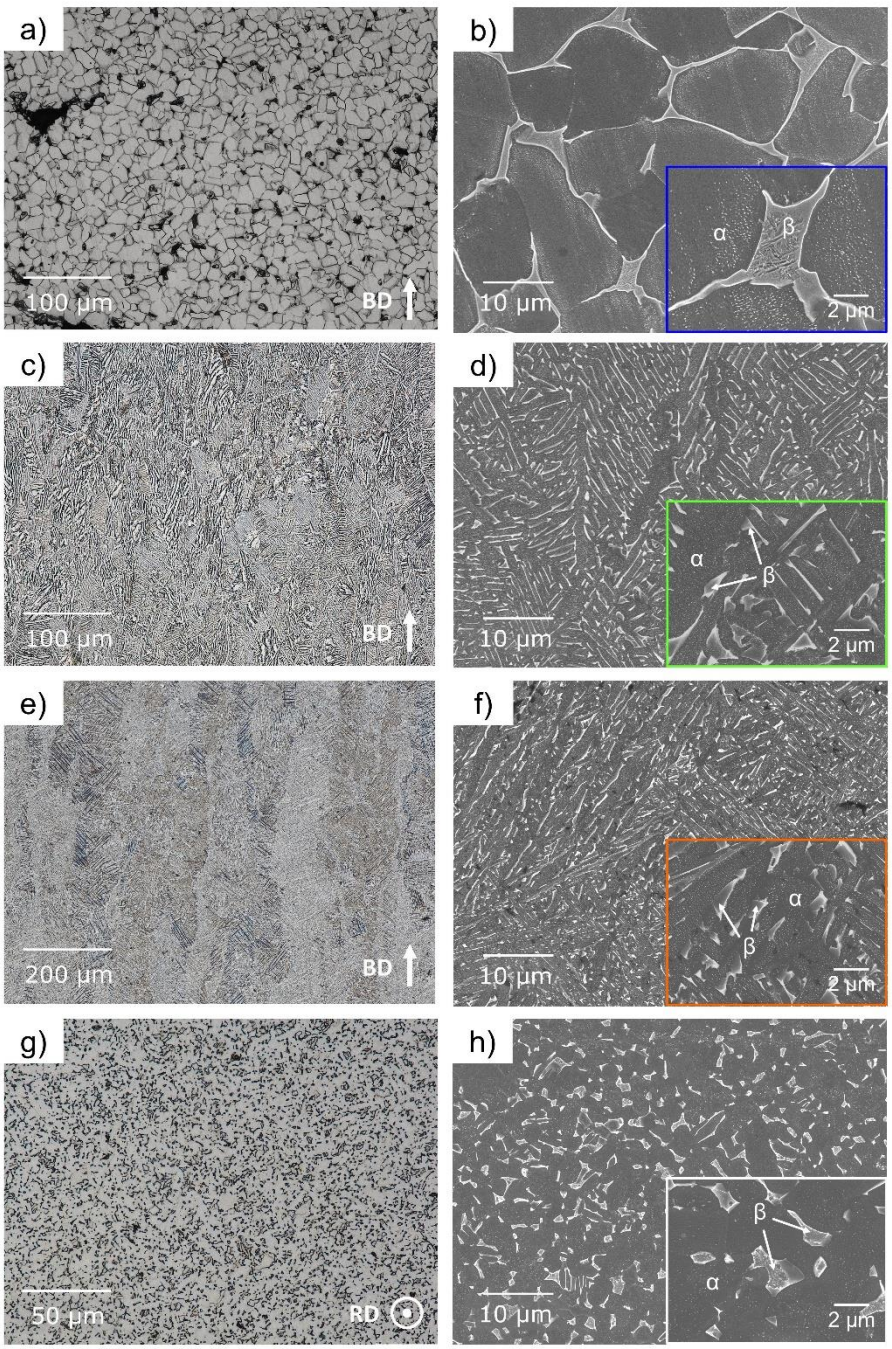

Figure 3 | Microstructures of the studied materials. OM and FESEM micrographs of (**a,b**) MEX, (**c,d**) EBM, (**e,f**) LPBF and (**g,h**) wrought Ti-6Al-4V specimens, respectively (etchant: Kroll's reagent); additively manufactured specimen micrographs are parallel to the building direction (BD), while wrought was analyzed orthogonally to the rolling direction.

Corrosion behavior assessment

Figure 4a and Figure 4b show the evolution of the open circuit potential (OCP) during the first 15 minutes of immersion and the subsequent potentiodynamic (PD) polarization curves, respectively. The Ti-6Al-4V alloy produced using different AM technologies exhibited comparable OCP values, with only minor

differences among the investigated conditions. In contrast, the polarization curves revealed a distinct behavior for the MEX specimens compared to those produced by EBM and LPBF. Indeed, the latters showed broad and stable passive region, followed by a sharp increase in current density at potentials above 1 V vs SCE, which are considerably higher than the typical corrosion potentials reported for Ti-6Al-4V alloys. These results are consistent with those reported by Sharma et al. for LPBF and conventionally cast Ti-6Al-4V alloys in NaCl solutions *[46]*. Conversely, the MEX material displayed a passive region characterized by higher current densities than the other technologies. Moreover, it exhibited current density with pronounced instabilities at high potentials, without a clear breakdown potential as observed in the other alloys. Overall, these results suggest that the MEX-produced alloy may exhibit lower corrosion resistance than the EBM and LPBF counterparts, despite maintaining passivity up to relatively high potentials.

However, PD polarization tests are not suitable for accurately quantifying the passive current density and, consequently, the corrosion rate of titanium alloys, since anodic polarization progressively increases the thickness of the passive film with increasing potential. Furthermore, PD technique is inherently non-stationary, not allowing the system to reach a true steady-state condition even with relatively low potential scan rates, and does not permit the time variable to be monitored independently from the applied potential. For these reasons, the stability of the passive film in Ti-6Al-4V alloy produced by different AM techniques was evaluated also through PS polarization tests. These tests were conducted at a potential of +500 mV vs. SCE, slightly higher than the commonly assumed OCP of titanium and its alloys in the human body *[47]*. Moreover, this potential is lower than the oxygen evolution potential at the pH of the used test solution and lies within the passive range of Ti-6Al-4V, as indicated by the dashed line in Figure 4b.

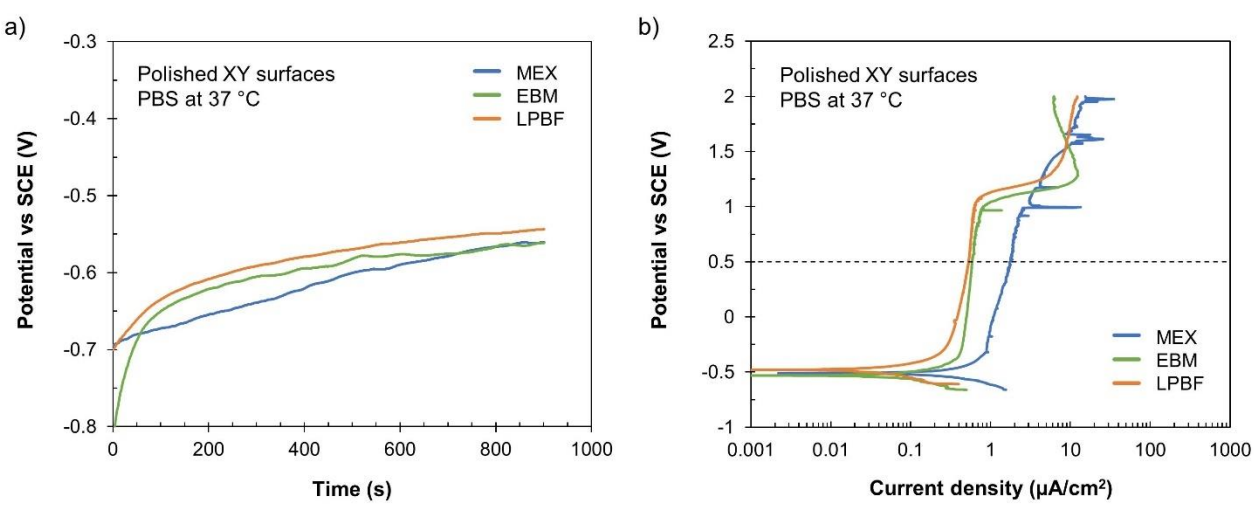

Figure 4 | Open circuit potential and anodic potentiodynamic polarization in de-aerated phosphate buffered saline (PBS). Representative (**a**) open circuit potential over time and (**b**) potential vs current density curves of polished AM alloys. Figure (**b**) also reports the potential further adopted for potentiostatic polarization tests (dashed line).

The curves shown in Figure 5 illustrate the current density evolution over time during the potentiostatic (PS) polarization tests in PBS, while Table 2 reports the corresponding current density values measured during the last 10 hours of immersion, denoted as i_{∞}. This results confirmed that all the investigated materials exhibited an excellent overall corrosion behavior in this environment with both as-built (Figure 5a) and polished (Figure 5b) surfaces. In fact, the tests carried out on the AB surfaces showed that stable

passive conditions were achieved after few hours of immersion and maintained throughout the whole test duration, despite some minor fluctuations. The current densities of AB specimens were calculated also considering the increase in the interface area (Sdr) due to roughness and waviness, as measured through confocal microscopy reconstructions (Table 1). These results confirmed that the native AM-produced oxide films, although formed under different conditions and environments, were still sufficiently protective in the chosen simulated body fluid, which can be considered as only mildly-aggressive for this class of materials. Moreover, only minor differences were observed among the different technologies in this condition, despite LPBF showed slightly lower stable current densities in the last hours of immersion. The differences observed in the PD tests – performed on polished specimens – were not detected in the unpolished condition. It is thus reasonable to assume that such differences arise from the exposure of defects induced by the polishing process.

Indeed, PS tests were also performed on polished XY surfaces (Figure 5b), to standardize the oxide formation conditions within the manufacturing technologies and to better highlight any differences due to microstructural or emerging porosity variations. Following polishing, all the materials showed steady passivity, although with higher initial values of current density than specimens with AB surfaces. This was due to the oxide formation kinetics, which required time to grow and stabilize after surface polishing. After polishing, the stable passivity current densities in the last hours of monitoring showed more evident differences among the investigated technologies (Figure 5b and Table 2). LPBF specimens showed lower current densities with respect to the other AM technologies. In particular, the slightly better corrosion behavior of LPBF-produced Ti-6Al-4V compared to the corresponding EBM samples confirmed what was already reported in previous studies *[14], [15], [48], [49]*. Conversely, polished MEX specimens exhibited passivity current densities higher than all other AM technologies during the whole test duration. Furthermore, MEX specimens exhibited a significant increase in current density following mechanical polishing (Figure 5a and Figure 5b). Although a comparable effect was also detected in the EBM- and LPBF-produced samples, its magnitude was sensibly lower with such materials. This effect confirmed that the increase in current observed for the MEX material can be ascribed to the exposure of macro-porosity induced by polishing step. Indeed, as previously demonstrated, MEX-produced material is characterized by the highest porosity levels, both in terms of areal distribution and defect size. Finally, the corrosion current densities of wrought Ti-6Al-4V were consistent with those of the EBM specimens (Table 2). Therefore, the material produced by MEX exhibited inferior corrosion resistance even with respect to the conventionally-manufactured alloy. However, MEX-produced Ti-6Al-4V exhibited a more than satisfactory overall corrosion behavior even for prolonged exposure, without evidence of passivity breakdown that would have resulted in significantly higher current densities.

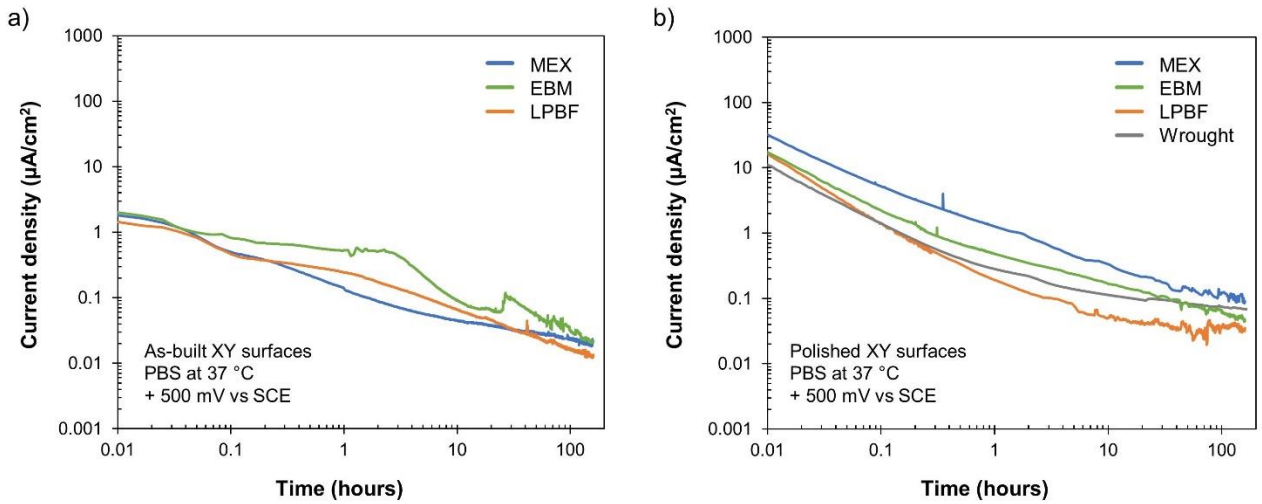

Figure 5 | Potentiostatic polarization in de-aerated phosphate buffered saline (PBS). Current density trend over time of the additively manufactured Ti-6Al-4V XY specimens with (**a**) as-built and (**b**) mechanically polished surfaces; polished wrought material curve is also reported as benchmark.

Table 2 | Average current densities in the last 10 hours of potentiostatic polarization for the different materials and surface conditions. No values are reported for the wrought material in the as-built surface condition, as this designation is not applicable.

Manufacturing technology	Surface condition	i_∞ (nA/cm^2)
MEX	As-built	28 ± 6
	Polished	139 ± 26
EBM	As-built	27 ± 3
	Polished	63 ± 8
LPBF	As-built	19 ± 3
	Polished	42 ± 7
Wrought	As-built	-
	Polished	69 ± 9

The average corrosion rates measured from short-term (ST) immersion tests are reported in Table 3. The ST immersion tests in isotonic solution highlighted the influence of environmental factors such as oxygen concentration and pH, as well as the impact of the process-related microstructure on the corrosion behavior of Ti-6Al-4V. The corrosion rates were negligible in neutral pH, while in acidified isotonic solution, especially without oxygen, corrosion rates became noticeable. These results confirmed the fundamental role of oxygen in promoting the passivation of the Ti-6Al-4V alloy also when produced by AM, in agreement with findings reported in previous studies on the conventionally-manufactured alloy *[44]*. As mentioned in the introduction, it is important to note that acidic environment with limited amount of

dissolved oxygen can occasionally occur within the human body in prostheses subjected to friction (e.g., hip joint and knee implants), where the simultaneous mechanical rupture of the oxide film and the presence of a crevice can occur *[18]*.

The average corrosion rates measured in these conditions showed no significant differences either among the specimens produced with different additive manufacturing technologies or between these and the wrought material. Furthermore, the corrosion rates assessed were relatively low, indicating a good corrosion behavior even in aggressive environments for all the tested materials.

Table 3 | Average corrosion rates during the short-term immersion tests for different environmental conditions (pH, dissolved oxygen).

	Average corrosion rate ($mg \cdot dm^{-2} \cdot day^{-1}$)			
	Neutral (pH 7)		Acidified (pH 0)	
	Aerated	De-aerated	Aerated	De-aerated
MEX	-	-	0.90 ± 0.18	54.7 ± 2.4
EBM	-	-	0.79 ± 0.14	48.4 ± 4.0
LPBF	-	-	0.61 ± 0.11	47.1 ± 3.9
Wrought	-	-	0.62 ± 0.13	53.7 ± 8.1

- = under measurement limit (0.30 $mg \cdot dm^{-2} \cdot day^{-1}$)

The FESEM images of the external surfaces before and after exposure to the acidified isotonic solution during the ST tests are shown in Figure 6. Corroded surface topography assessed via atomic force microscopy (AFM) is also shown. All the specimens exhibited a macroscopically homogeneous corrosion over the exposed surfaces, with slight but noticeable selective corrosion. In particular, the α phase was found to preferentially corrode, in agreement with other studies on conventional Ti-6Al-4V alloy in similar environments *[44]*. Preferential corrosion of the α phase was particularly evident in the case of the MEX and wrought specimens (Figure 6b,h), where emerging β phase regions were clearly visible, indicating its lower degradation rate than the α phase. Conversely, enhanced α-phase degradation was less easily recognizable with EBM and LPBF specimens (Figure 6d,f) due to their finer microstructure, despite the corrosion attacks clearly followed the lamellar microstructure previously observed in the microstructural characterization.

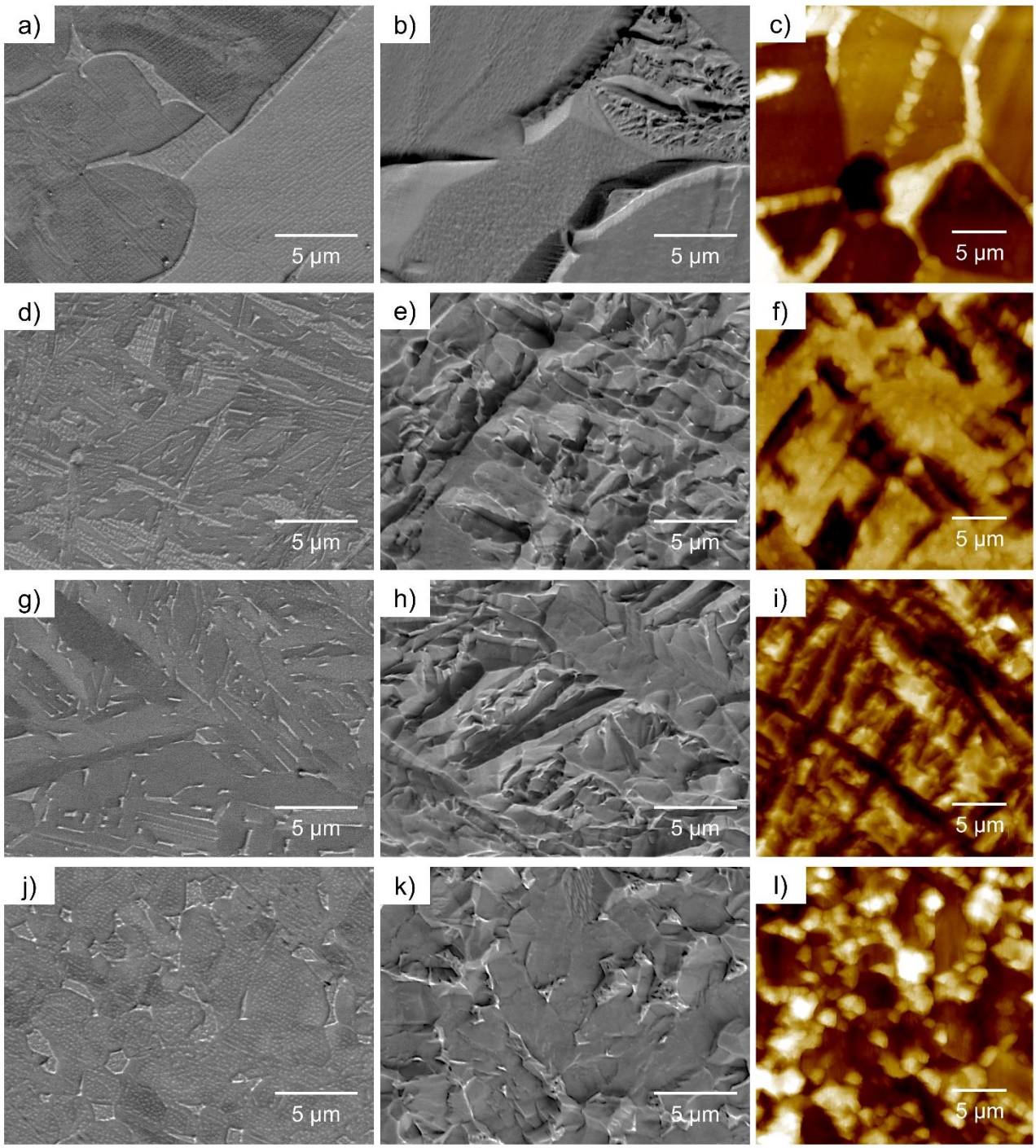

Figure 6 | Corrosion morphologies after de-aerated, acidified isotonic solution ST immersion tests. Backscattered FESEM micrographs of the (**a,d,g,j**) polished and (**b,e,h,k**) corroded surfaces, and (**c,f,i,l**) AFM topography images of the corroded surfaces of (**a,b,c**) MEX, (**d,e,f**) EBM, (**g,h,i**) LPBF and (**j,k,l**) wrought Ti-6Al-4V specimens (AFM color bar range: 1200 nm).

The different corrosion behavior of α and β phases was further investigated by means of scanning Kelvin probe force microscopy (SKPFM) analyses, which revealed a consistent higher Volta potential of the β phase with respect to the α phase in all the studied materials (Figure 7).

Such results are in agreement with those previously reported by Li et al. *[44]* and Zhang et al. *[50]* on conventionally-manufactured Ti-6Al-4V. In particular, Li et al. *[44]* used the Volta potential of the α and β phases to explain the different electrochemical behavior of the two phases and their distinct tendency toward passivation. The same authors demonstrated that, although α phase exhibits higher passivation efficiency – due to its overall lower concentration of alloying elements compared to the β phase – it also develops an oxide film that, under de-aerated conditions, is weakened by its higher aluminum content with respect to the β phase. Furthermore, assuming that the Volta potential can be correlated with the nobility of the phases *[51]*, the higher Volta potential of the β phase confirmed the thermodynamic prerequisite for the onset of micro-galvanic coupling between the α and β phases. Under stable passive conditions, this effect is likely hindered in titanium and its alloys by the presence of a highly insulating oxide film. However, under conditions of imperfect passivity – such as the acidic and reducing de-aerating environments considered in this study – it cannot be excluded that this corrosion mechanism may contribute to the selective attack of the α phase.

In this study, the different AM microstructures and the slight compositional variations showed only minor effect on Volta potential values, obtaining comparable maximum differences (ΔE_{Volta}) between α and β phases, in the range of 205-217 mV. The different morphologies and arrangements of the α and β phases among technologies led only to different potential distributions and different preferential paths for selective attacks (Figure 6).

Furthermore, it is important to emphasize that the extent of selective corrosion attacks observed in this study was significantly lower than that reported for this alloy in other human body-simulating environments, such as studies involving hydrogen peroxide and cathodic activation, in which a markedly different morphology was observed *[16]*, *[18]*. In such environments, Prestat et al. *[16]* reported a pronounced dissolution of the β phase, which was ascribed to the reduced passivation capability of this phase under the given conditions, although the underlying mechanism remained not fully clarified. Therefore, the contradictory findings available in the scientific literature indicate the difficulty of defining *a priori* the corrosion behavior of the α and β phases, whose response can vary markedly depending on the specific environmental conditions.

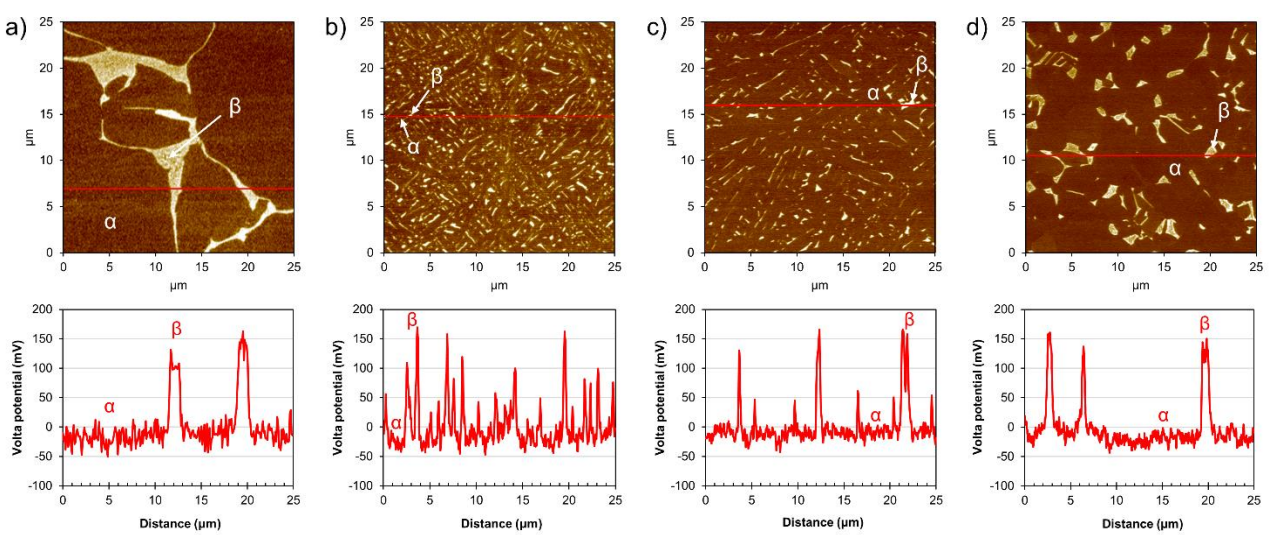

Figure 7 | Scanning Kelvin probe force microscopy (SKPFM) results. Volta potential maps and related line scans highlighting the different α+β duplex microstructures of (**a**) MEX, (**b**) EBM, (**c**) LPBF and (**d**) wrought Ti-6Al-4V specimens (color bar range: 300 mV).

The results of the long-term (LT) immersion tests in aerated acidified isotonic solution (pH 0) revealed some relevant differences between the additively-manufactured and wrought specimens, as well as between MEX and EBM/LPBF specimens. Indeed, the wrought Ti-6Al-4V specimens showed average corrosion rates of 0.20 ± 0.07 $mg \cdot dm^{-2} \cdot day^{-1}$, which were the lowest among all the studied manufacturing technologies. EBM and LPBF specimens exhibited corrosion rates moderately higher than wrought material, although within the same order of magnitude (0.34 ± 0.13 and 0.39 ± 0.09 $mg \cdot dm^{-2} \cdot day^{-1}$, respectively). Finally, the average corrosion rates of the MEX specimens were approximately three times those of the EBM and LPBF specimens, and five times those of the wrought specimens (1.02 ± 0.31 $mg \cdot dm^{-2} \cdot day^{-1}$). It is also important to emphasize that EBM, LPBF and wrought specimens exhibited lower average corrosion rates in the LT tests if compared to ST tests (Table 3) under the same conditions (aerated, pH 0), indicating the propensity for passivation. Conversely, MEX specimens' average corrosion rates during the LT tests were comparable to the corresponding ST tests, suggesting a roughly constant corrosion rate over time.

These results were confirmed by the observation of the corroded specimens, shown in Figure 8. Examining the external surfaces of the specimens (Figure 8a,b,c,d), the wrought material exhibited slight generalized corrosion without significant localized attacks, consistently with its average corrosion rates. In contrast, the EBM and LPBF specimens showed similar corroded surfaces characterized by occasional pits, with depth in the order of 50-100 μm, which justified their higher average corrosion rates with respect to the wrought material. LPBF specimens exhibited slightly bigger localized attacks than EBM counterparts. It is likely that localized attacks originated from the emerging porosities, exposed during the polishing process, which may provide a preferential site for the initiation of corrosion. However, specific studies are needed to confirm the relationship between porosity and the onset of localized corrosion for these AM techniques.

The MEX specimens, on the other hand, showed evident corrosion attacks on most of the exposed surface, but especially at the ends where the porous network was directly exposed to the environment. In fact, by examining the cross-section of the corroded specimen (Figure 8e), it was possible to observe that on the contour side there was only slight, uniform corrosion over almost the entire surface. In contrast, the upper and lower XY surfaces (Figure 8g), and especially the Z surface where the contour was removed by polishing (Figure 8f), showed severe material degradation, also manifested by the increased size of the porosities compared to the internal, non-corroded region of the core. On XY-oriented surfaces, corrosion was mostly limited to the outer porous layer, suggesting partial pores interconnection between adjacent layers. In contrast, the direct exposure of porous network on Z-oriented surfaces facilitated electrolyte penetration and promoted corrosion propagation. All these observations indicated that the exposure of the macro-defects network triggered the onset of corrosion phenomena, drastically reducing the corrosion resistance of the Ti-6Al-4V alloy. Furthermore, this consideration is also consistent with the differences observed in the electrochemical tests performed in PBS between unpolished MEX specimens (showing no emerging porosity) and polished ones (exhibiting emerging porosity).

By examining the cross-section of the corroded MEX specimen at higher magnifications (Figure 8h,i), a locally homogeneous corrosion was observed, only slightly affected by the selective corrosion phenomena between the α and β phases previously assessed in the ST tests. Therefore, following prolonged exposure times, the corrosion was found to be more influenced by the presence of the defects than by the process-related microstructure. These results highlighted the need to adopt appropriate strategies to reduce the

overall porosity in MEX specimens, such as optimizing feedstock, printing parameters and debinding/sintering processes and/or implementing specific post-printing treatments. Indeed, the presence of large, endogenous defects which are furthermore mutually interconnected appeared to be the main feature affecting the corrosion resistance of Ti-6Al-4V alloy produced by MEX, also limiting its potential implementation in the biomedical field or other critical engineering applications.

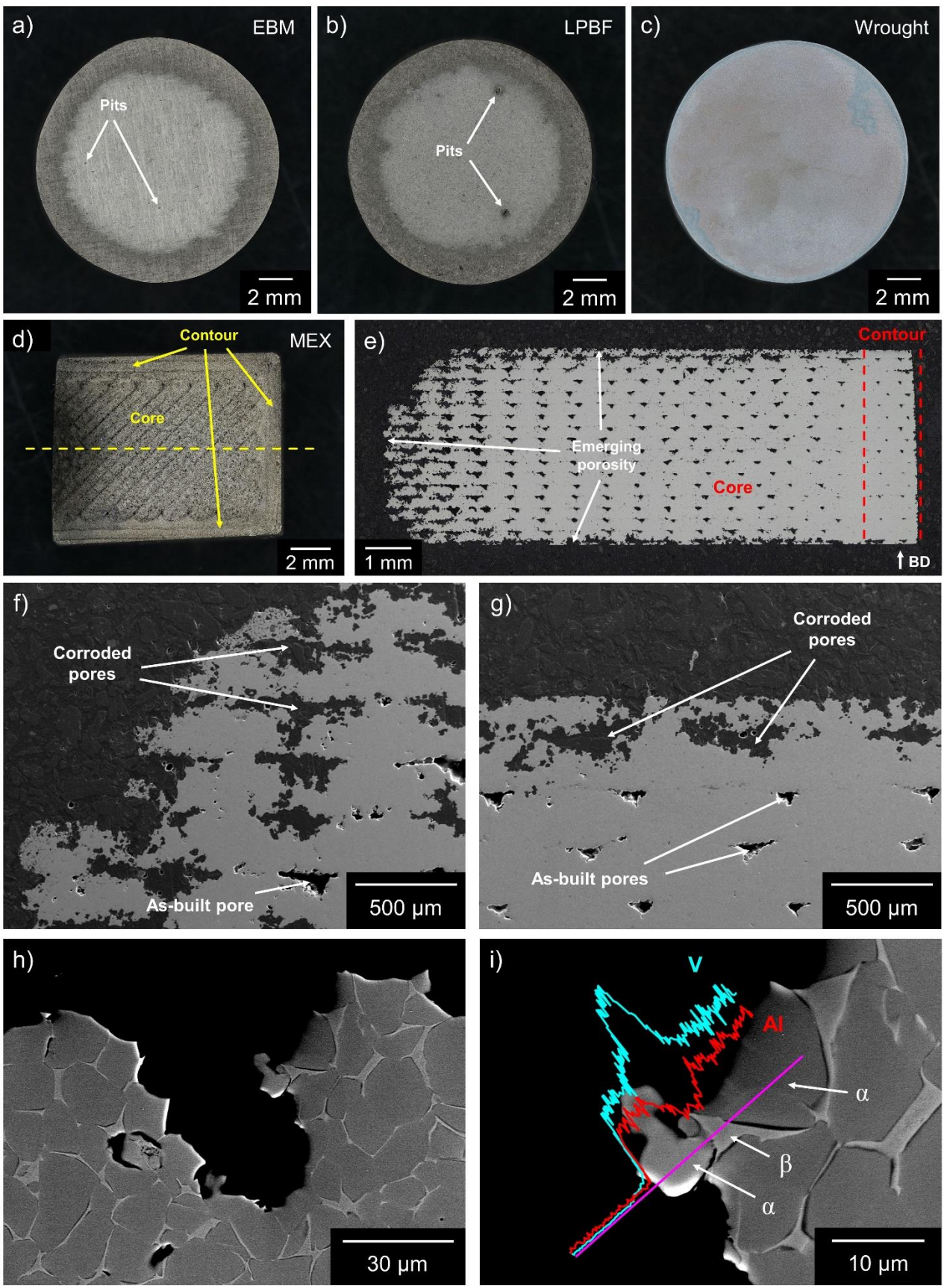
a)
EBM
Pits
2 mm
b)
LPBF
Pits
2 mm
c)
Wrought
2 mm
d)
Contour
MEX
Core
2 mm
e)
Contour
Emerging porosity
Core
1 mm
BD
f)
Corroded pores
As-built pore
500 µm
g)
Corroded pores
As-built pores
500 µm
h)
30 µm
i)
V
Al
α
β
α
10 µm

Figure 8 | Corrosion morphologies after long-term immersion tests in aerated, acidified isotonic solution. Low magnification OM images of (**a**) EBM, (**b**) LPBF, (**c**) wrought and (**d**) MEX Ti-6Al-4V specimens after exposure; figure (**d**) also includes the cutting line (dashed yellow line) used to obtain the metallographic section of the MEX specimen subsequently analyzed: (**e**) OM macro image of the metallographic section parallel to the building direction (BD), (**f,g**) FESEM secondary electron micrographs showing pores corrosion morphology on Z and XY surfaces, respectively, and (**g,i**) FESEM backscattered electron micrographs with EDS line scan of Al and V.

Overall, this study highlighted evident process-dependent differences in external surfaces morphology, porosity, and microstructural features among different AM routes. All AM alloys displayed high surface waviness and powder-related roughness, although EBM and LPBF showed more pronounced anisotropy between XY and Z surfaces than MEX. Porosity was also strongly process-dependent: MEX specimens contained periodic, elongated macro-defects, whereas EBM and LPBF alloys exhibited only small, spherical pores. All materials were characterized by an α+β microstructure; however, MEX process produced equiaxed α grains with β phase at grain boundary - resembling wrought Ti-6Al-4V - while EBM and LPBF led to lamellar microstructures. Despite these differences, all AM alloys demonstrated excellent corrosion resistance in PBS, in both as-built and polished conditions, with stable passive currents comparable to wrought material. The only notable deviation was the slightly higher passive current density measured for polished MEX specimens, likely due to the exposure of their characteristic macro-defects. Volta potential maps and corrosion morphologies proved that the arrangement of α and β phases plays a role in driving selective attack, which was observed only after aggressive exposure to acidic, reducing conditions and remained very limited in extent. Under prolonged acidic immersion, however, porosity became the dominant factor controlling degradation, confirming its detrimental role. This effect was most evident in MEX specimens, whose macro-defect network acted as preferential path for corrosion propagation. This aspect underscores that while fusion-based AM techniques (EBM, LPBF) are able to produce microstructures and defect levels compatible with high corrosion resistance, the intrinsic porosity of sinter-based MEX processing remains a key limitation for applications requiring exposure to harsh environments.

Methods

Materials

The tests were carried out on Ti-6Al-4V alloy manufactured with three different AM technologies – specifically MEX, EBM and LPBF – as well as on wrought material, taken as a reference. Prismatic specimens 5 mm×10 mm×15 mm were used for the Ti-6Al-4V alloy obtained through MEX, whereas cylindrical specimens 15 mm diameter, 5 mm height were adopted for EBM, LPBF and wrought alloys.

MEX specimens were manufactured depositing a metal-polymer feedstock filament, provided by Element 22 GmbH, adopting a ±45° deposition strategy in the inner core region, with a 3 stripes-thick contour parallel to the specimen lateral sides. Both core and contour regions were produced with 100% infill, 300 µm layer thickness, 50 °C print bed temperature, 160 °C nozzle temperature and 15 mm/s printing speed. The resulting green parts were then debound and sintered, to remove the polymeric binder and to consolidate the metallic powders, according to the process patented by Element 22 GmbH. EBM samples were produced with an Arcam A2X apparatus with a printing chamber kept in vacuum and a building temperature close to 700 °C. The operating parameters for EBM system were optimized by the machine manufacturer and remain undisclosed. LPBF specimens were manufactured using an EOS M270 Dual Mode equipment with an Yb laser source and operating in Ar atmosphere, with 170 W laser power, 1250 mm/s scanning speed, 30 µm layer thickness and 100 µm hatching distance. The conventionally-

manufactured material was supplied by Titalia S.p.a. in the form of a 16 mm diameter bar in annealed condition (750 °C for 1 h).

The AM specimens were tested in AB condition except for the LPBF specimens, which were subjected to heat treatment (680 °C for 4 h in high-vacuum, furnace cooling at roughly 2 °C/min) in order to remove the high residual stresses and brittle martensitic α'-phase, which are typical of the AB condition.

The chemical compositions of the specimens and the AM feedstock powders granulometry are reported in Table 4. It is important to emphasize that the oxygen, nitrogen, hydrogen and carbon contents of the MEX-processed material here reported are the nominal values referred to the feedstock powders, as a direct measurement in the printed specimen can be difficult due to the macro-defects discussed in the results. The granulometry of the feedstock powders is reported in terms of volume percentiles D(10), D(50), and D(90).

Table 4 | Chemical compositions (wt.%) and particle size distributions of the studied materials.

Manufacturing technology	Element (wt.%)								Particle size (μm)		
	Ti	Al	V	O	N	H	Fe	C	D(10)	D(50)	D(90)
MEX	Bal.	6.19	3.60	<0.35	<0.035	<0.015	0.16	<0.045	4	7	13
EBM	Bal.	6.41	3.86	0.09	0.010	0.002	0.19	0.02	45	62	84
LPBF	Bal.	5.86	3.99	0.08	0.003	0.002	0.18	0.01	22	33	47
Wrought	Bal.	6.24	4.23	0.17	0.012	0.001	0.14	0.01	-	-	-

Microstructure, defects and surfaces characterization

Microstructure and defects were investigated using a Keyence VHX-7100 digital-OM and a Zeiss Sigma 300 FESEM equipped with an Oxford x-act probe for energy-dispersive X-ray spectroscopy (EDS). The microstructure was further analyzed by means of SKPFM under ambient condition using a Park Systems NX10 AFM equipped with a Pt-coated rectangular conductive cantilever (ElectriMulti75-G) characterized by 75 kHz resonant frequency and 3 N/m spring constant. Scans were performed at a 0.05 Hz scan rate, mapping 25 μm×25 μm areas and adopting dynamic mode, single-pass methodology.

The specimens were mechanically ground with SiC emery papers up to 1200 grit and then polished with a 30 nm silica suspension. Before OM and FESEM analyses, the specimen microstructures were highlighted with Kroll's reagent for approximately 5 seconds. AM alloys volumetric porosity was measured with ImageJ image correlation software on OM micrographs, obtained on polished and un-etched cross section. AM-generated surfaces, both vertical (Z) and horizontal (XY), were 3D reconstructed with a Sensofar S Neox optical-confocal profilometer, performing analyses with a green led on a 6×6 grid at 50X magnifications, which corresponds to a 1.255×1.667 mm^2 area, and a 0.20 μm vertical step. The experimental point clouds were then processed with SensoVIEW software according to ISO 25178 standard, calculating the values of average surface roughness (Sa), peak-to-peak surface roughness (Sz) and developed interfacial area ratio (Sdr). These parameters were calculated considering the effect of both local roughness and long-range waviness, applying a standard short-wavelength filter (λ_S) equal to 2.5 μm.

Corrosion behavior assessment

The corrosion behavior of the different alloys was evaluated through both electrochemical and immersion tests. The test solutions were selected with the primary purpose of highlighting differences among alloys produced with different manufacturing technologies and/or assessing the effect of environmental parameters, without aiming to faithfully reproducing real physiological conditions.

The overall corrosion behavior was assessed via PD polarization tests on XY polished surfaces, while PS polarization were performed on both as-built and polished XY surfaces. The tests were carried out using an Ivium Compactstat potentiostat and a standard ASTM G5 1 L cell equipped with graphite counter electrodes and a saturated calomel electrode (SCE) as a reference electrode. The used test solution was a de-aerated phosphate-buffered saline (PBS) solution, containing 8.74 g/L NaCl, 0.35 g/L $NaHCO_3$, 0.06 g/L Na_2HPO_4 and 0.06 g/L NaH_2PO_4 (pH 7.4) and kept at 37±1 °C. The test solution was de-aerated for at least 1 hour before the test via nitrogen bubbling, maintained even during the test. Although dissolved oxygen is obviously present within the human body, deoxygenated test solution was adopted in compliance with ISO 10993-15. PD tests were carried out after OCP monitoring for 15 minutes, scanning from -100 mV vs OCP up to 2 V vs SCE with 10 mV/min scan rate. PS tests were carried out for 160 hours anodically polarizing the specimens at +500 mV vs SCE, which is slightly higher than the commonly assumed OCP of Ti-alloys in the human body *[47]*.

Immersion tests were carried out in isotonic solution (9 g/L NaCl) at 37±1 °C, prescribed by ISO 10993-15 standard as possible media for simulating physiological chloride concentrations. The immersion campaign included ST (18 hours) and LT (1000 hours) exposures. The isotonic solution was selected due to its ease of acidification, enabling the assessment of pH effects on corrosion phenomena.

ST immersion tests were carried out to evaluate the effect of the production technology and oxygen content/pH on selective corrosion, exposing polished specimens in aerated and de-aerated isotonic solution, as well as in aerated and de-aerated acidified isotonic solution, acidified at pH 0 by HCl addition. The adopted pH is below the physiological range commonly associated with inflammatory or crevice corrosion conditions and was intentionally selected to emphasize the differences between the investigated alloys. The volume of solution to exposed surface ratio was 15 mL/cm^2. The specimens were measured before testing with a Vernier caliper and weighted with an analytical balance (0.00001 g sensitivity), in order to assess the average corrosion rates from weight loss. Considering the balance sensitivity, the test duration, and the minimum specimen exposed surface, this experimental setup allowed the measurement of average corrosion rates greater than or equal to approximately 0.3 $mg \cdot dm^{-2} \cdot day^{-1}$. The corrosion morphologies were analyzed with FESEM and AFM. Topographical analyses were performed using a resonant cantilever (CONTSCR) operating at 23 kHz, with a spring constant of 0.2 N/m and an aluminum tip. Measurements were carried out in non-contact mode over a scanning area of 25 µm ×25 µm.

LT immersion tests were carried out in aerated, acidified isotonic solution. The procedures for conducting these tests were identical to those of the ST immersion tests, except for the solution volume/specimen exposed surface ratio of 2 mL/cm^2. For the LT immersion tests, the MEX specimens were polished to completely remove the contour layers at one end, in order to observe the effect of environment exposure on the porous network in the core region.

Data availability

All data generated or analyzed during this study are included in this published article.

Acknowledgements

Financed by the European Union - NextGenerationEU (National Sustainable Mobility Center CN00000023, Italian Ministry of University and Research Decree n. 1033 - 17/06/2022, Spoke 5 - Light vehicle and active mobility, and Spoke 11 - Innovative Materials & Lightweighting). The opinions expressed are those of the authors only and should not be considered as representative of the European Union or the European Commission's official position. Neither the European Union nor the European Commission can be held responsible for them.

Author contributions

S.L.: conceptualization, methodology, project administration, resources, supervision, validation, funding acquisition, writing – review & editing. L.N.: data curation, investigation, methodology, visualization, validation, writing – original draft. T.P.: data curation, investigation, validation, writing – original draft. M.L.: conceptualization, resources, writing – review & editing. F.S.: conceptualization, resources, funding acquisition, writing – review & editing. C.S.: conceptualization, resources, writing – review & editing. M.C.: conceptualization, methodology, project administration, resources, supervision, validation, writing – review & editing.

Competing interests

The authors declare no competing financial or non-financial interests.

References

[1] H. D. Nguyen et al., "A critical review on additive manufacturing of Ti-6Al-4V alloy: microstructure and mechanical properties," J. Mater. Res. Technol., vol. 18, pp. 4641–4661, May 2022, doi: 10.1016/j.jmrt.2022.04.055.

[2] F. Trevisan et al., "Additive manufacturing of titanium alloys in the biomedical field: processes, properties and applications," J. Appl. Biomater. Funct. Mater., vol. 16, no. 2, pp. 57–67, Apr. 2018, doi: 10.5301/jabfm.5000371.

[3] Q. Chen and G. A. Thouas, "Metallic implant biomaterials," Mater. Sci. Eng. R Rep., vol. 87, pp. 1–57, Jan. 2015, doi: 10.1016/j.mser.2014.10.001.

[4] S. Liu and Y. C. Shin, "Additive manufacturing of Ti6Al4V alloy: A review," Mater. Des., vol. 164, p. 107552, Feb. 2019, doi: 10.1016/j.matdes.2018.107552.

[5] D. Mahmoud and M. A. Elbestawi, "Lattice Structures and Functionally Graded Materials Applications in Additive Manufacturing of Orthopedic Implants: A Review," J. Manuf. Mater. Process., vol. 1, no. 2, Art. no. 2, Dec. 2017, doi: 10.3390/jmmp1020013.

[6] T. Majumdar, N. Eisenstein, J. E. Frith, S. C. Cox, and N. Birbilis, "Additive Manufacturing of Titanium Alloys for Orthopedic Applications: A Materials Science Viewpoint," Adv. Eng. Mater., vol. 20, no. 9, p. 1800172, 2018, doi: 10.1002/adem.201800172.

[7] E. Davoodi et al., "Additively manufactured metallic biomaterials," Bioact. Mater., vol. 15, pp. 214–249, Dec. 2021, doi: 10.1016/j.bioactmat.2021.12.027.

[8] S. C. Altıparmak, V. A. Yardley, Z. Shi, and J. Lin, “Extrusion-based additive manufacturing technologies: State of the art and future perspectives,” J. Manuf. Process., vol. 83, pp. 607–636, Nov. 2022, doi: 10.1016/j.jmapro.2022.09.032.

[9] C. Sergi et al., “Ti6Al4V Components by Bound Metal Deposition and Competitive with Metal Injection Molded Parts: Optimization of the Printing Parameters,” Adv. Eng. Mater., vol. 27, no. 10, p. 2402813, 2025, doi: 10.1002/adem.202402813.

[10] A. I. Nurhudan, S. Supriadi, Y. Whulanza, and A. S. Saragih, “Additive manufacturing of metallic based on extrusion process: A review,” J. Manuf. Process., vol. 66, pp. 228–237, Jun. 2021, doi: 10.1016/j.jmapro.2021.04.018.

[11] H. Ramazani and A. Kami, “Metal FDM, a new extrusion-based additive manufacturing technology for manufacturing of metallic parts: a review,” Prog. Addit. Manuf., vol. 7, no. 4, pp. 609–626, Aug. 2022, doi: 10.1007/s40964-021-00250-x.

[12] S. Lorenzi, G. D’Urso, L. Nani, M. Quarto, S. Fest-Santini, and T. Pastore, “Effect of the deposition strategy and endogenous defect pattern on the plastic deformability and the fracture mechanism of 316L stainless steel obtained using material extrusion,” Eng. Fail. Anal., vol. 171, p. 109395, Apr. 2025, doi: 10.1016/j.engfailanal.2025.109395.

[13] A. Carrozza et al., “A comparative analysis between material extrusion and other additive manufacturing techniques: Defects, microstructure and corrosion behavior in nickel alloy 625,” Mater. Des., vol. 225, p. 111545, Jan. 2023, doi: 10.1016/j.matdes.2022.111545.

[14] M. Cabrini et al., “Influence of surface finishing and heat treatments on the corrosion resistance of LPBF-produced Ti-6Al-4V alloy for biomedical applications,” J. Mater. Process. Technol., vol. 308, p. 117730, Oct. 2022, doi: 10.1016/j.jmatprotec.2022.117730.

[15] A. Carrozza, M. Cabrini, S. Lorenzi, M. Lombardi, and T. Pastore, “Improving the Corrosion Performance of LPBF- and EBM-Processed Ti-6Al-4V by Chemical Pickling,” Eng. Sci., vol. Volume 26 (December 2023), no. 2, p. 985, Oct. 2023.

[16] M. Prestat, F. Vucko, L. Holzer, and D. Thierry, “Microstructural aspects of Ti6Al4V degradation in H2O2-containing phosphate buffered saline,” Corros. Sci., vol. 190, p. 109640, Sep. 2021, doi: 10.1016/j.corsci.2021.109640.

[17] W. Xu, B. Zhang, O. Addison, X. Wang, B. Hou, and F. Yu, “Mechanically-assisted crevice corrosion and its effect on materials degradation,” Corros. Commun., vol. 11, pp. 23–32, Sep. 2023, doi: 10.1016/j.corcom.2023.01.002.

[18] M. A. Kurtz, P. Khullar, and J. L. Gilbert, “Cathodic activation and inflammatory species are critical to simulating in vivo Ti-6Al-4V selective dissolution,” Acta Biomater., vol. 149, pp. 399–409, Sep. 2022, doi: 10.1016/j.actbio.2022.07.020.

[19] J. Toledano-Serrabona et al., “Ion release and local effects of titanium metal particles from dental implants: An experimental study in rats,” J. Periodontol., vol. 94, no. 1, pp. 119–129, 2023, doi: 10.1002/JPER.22-0091.

[20] M. Kawahara and M. Kato-Negishi, “Link between Aluminum and the Pathogenesis of Alzheimer′s Disease: The Integration of the Aluminum and Amyloid Cascade Hypotheses,” Int. J. Alzheimer’s Dis., vol. 2011, no. 1, p. 276393, 2011, doi: 10.4061/2011/276393.

[21] G. Sander et al., “Corrosion of Additively Manufactured Alloys: A Review,” Corrosion, vol. 74, no. 12, pp. 1318–1350, Oct. 2018, doi: 10.5006/2926.

[22] C. Xu, J. Qi, L. Zhang, Q. Liu, and L. Ren, “Material extrusion additive manufacturing of Ti6Al4V bio-inspired bone implants with tunable Young’s modulus,” Addit. Manuf., vol. 78, p. 103884, Sep. 2023, doi: 10.1016/j.addma.2023.103884.

[23] L. García de la Cruz, P. Alvaredo, J. M. Torralba, and M. Campos, “Material extrusion: A promising tool for processing CoCrMo alloy with excellent wear resistance for biomedical applications,” Mater. Des., vol. 244, p. 113089, Aug. 2024, doi: 10.1016/j.matdes.2024.113089.

[24] F. Cabanettes et al., “Topography of as built surfaces generated in metal additive manufacturing: A multi scale analysis from form to roughness,” Precis. Eng., vol. 52, pp. 249–265, Apr. 2018, doi: 10.1016/j.precisioneng.2018.01.002.

[25] M. C. Kayacan et al., “Monitoring the osseointegration process in porous Ti6Al4V implants produced by additive manufacturing: an experimental study in sheep,” J. Appl. Biomater. Funct. Mater., vol. 16, no. 2, pp. 68–75, Apr. 2018, doi: 10.5301/jabfm.5000385.

[26] L. Le Guehennec, M.-A. Lopez-Heredia, B. Enkel, P. Weiss, Y. Amouriq, and P. Layrolle, “Osteoblastic cell behaviour on different titanium implant surfaces,” Acta Biomater., vol. 4, no. 3, pp. 535–543, May 2008, doi: 10.1016/j.actbio.2007.12.002.

[27] C. Mas-Moruno, B. Su, and M. J. Dalby, “Multifunctional Coatings and Nanotopographies: Toward Cell Instructive and Antibacterial Implants,” Adv. Healthc. Mater., vol. 8, no. 1, p. 1801103, 2019, doi: 10.1002/adhm.201801103.

[28] A. Wennerberg and T. Albrektsson, “Effects of titanium surface topography on bone integration: a systematic review,” Clin. Oral Implants Res., vol. 20 Suppl 4, pp. 172–184, Sep. 2009, doi: 10.1111/j.1600-0501.2009.01775.x.

[29] A. Palmquist, M. Jolic, E. Hryha, and F. A. Shah, “Complex geometry and integrated macro-porosity: Clinical applications of electron beam melting to fabricate bespoke bone-anchored implants,” Acta Biomater., vol. 156, pp. 125–145, Jan. 2023, doi: 10.1016/j.actbio.2022.06.002.

[30] K. Anselme and M. Bigerelle, “Topography effects of pure titanium substrates on human osteoblast long-term adhesion,” Acta Biomater., vol. 1, no. 2, pp. 211–222, Mar. 2005, doi: 10.1016/j.actbio.2004.11.009.

[31] C. Suwanpreecha and A. Manonukul, “A Review on Material Extrusion Additive Manufacturing of Metal and How It Compares with Metal Injection Moulding,” Metals, vol. 12, no. 3, Art. no. 3, Mar. 2022, doi: 10.3390/met12030429.

[32] M. Quarto and C. Giardini, “Additive manufacturing of metal filament: when it can replace metal injection moulding,” Prog. Addit. Manuf., vol. 8, no. 3, pp. 561–570, Jun. 2023, doi: 10.1007/s40964-022-00348-w.

[33] M. Sadaf, M. Bragaglia, L. Slemenik Perše, and F. Nanni, “Advancements in Metal Additive Manufacturing: A Comprehensive Review of Material Extrusion with Highly Filled Polymers,” J. Manuf. Mater. Process., vol. 8, no. 1, p. 14, Feb. 2024, doi: 10.3390/jmmp8010014.

[34] Y.-K. Kim, S.-J. Youn, K.-R. Lim, and Y.-S. Na, “Fused deposition modeling of Inconel 625 alloy: Effect of hot isostatic pressing on the microstructure and tensile properties,” Mater. Sci. Eng. A, vol. 897, p. 146328, Apr. 2024, doi: 10.1016/j.msea.2024.146328.

[35] R. Eickhoff, S. Antusch, D. Nötzel, and T. Hanemann, “New Partially Water-Soluble Feedstocks for Additive Manufacturing of Ti6Al4V Parts by Material Extrusion,” Materials, vol. 16, no. 8, Art. no. 8, Jan. 2023, doi: 10.3390/ma16083162.

[36] M. C. Brennan, J. S. Keist, and T. A. Palmer, “Defects in Metal Additive Manufacturing Processes,” J. Mater. Eng. Perform., vol. 30, no. 7, pp. 4808–4818, Jul. 2021, doi: 10.1007/s11665-021-05919-6.

[37] X. P. Ren et al., “A comparative study on mechanical properties of Ti–6Al–4V alloy processed by additive manufacturing vs. traditional processing,” Mater. Sci. Eng. A, vol. 817, p. 141384, Jun. 2021, doi: 10.1016/j.msea.2021.141384.

[38] A. Carrozza et al., “Effect of Aging and Cooling Path on the Super β-Transus Heat-Treated Ti-6Al-4V Alloy Produced via Electron Beam Melting (EBM),” Materials, vol. 15, no. 12, Art. no. 12, Jan. 2022, doi: 10.3390/ma15124067.

[39] C. de Formanoir, S. Michotte, O. Rigo, L. Germain, and S. Godet, “Electron beam melted Ti–6Al–4V: Microstructure, texture and mechanical behavior of the as-built and heat-treated material,” Mater. Sci. Eng. A, vol. 652, pp. 105–119, Jan. 2016, doi: 10.1016/j.msea.2015.11.052.

[40] T. Zhang and C.-T. Liu, “Design of titanium alloys by additive manufacturing: A critical review,” Adv. Powder Mater., vol. 1, no. 1, p. 100014, Jan. 2022, doi: 10.1016/j.apmate.2021.11.001.

[41] P. A. Hooper, “Melt pool temperature and cooling rates in laser powder bed fusion,” Addit. Manuf., vol. 22, pp. 548–559, Aug. 2018, doi: 10.1016/j.addma.2018.05.032.

[42] W. Xu et al., “Additive manufacturing of strong and ductile Ti–6Al–4V by selective laser melting via in situ martensite decomposition,” Acta Mater., vol. 85, pp. 74–84, Feb. 2015, doi: 10.1016/j.actamat.2014.11.028.

[43] Y.-W. Cui et al., “Metastable pitting corrosion behavior of laser powder bed fusion produced Ti-6Al-4V in Hank’s solution,” Corros. Sci., vol. 203, p. 110333, Jul. 2022, doi: 10.1016/j.corsci.2022.110333.

[44] J. Li, Y. He, W. Shi, S. Xiang, and W. Gao, “Different passivation behavior between α and β phases of Ti-6Al-4V in HCl solutions under oxygenated/deoxygenated conditions,” Appl. Surf. Sci., vol. 604, p. 154539, Dec. 2022, doi: 10.1016/j.apsusc.2022.154539.

[45] L. R. Zeng, H. L. Chen, X. Li, L. M. Lei, and G. P. Zhang, “Influence of alloy element partitioning on strength of primary α phase in Ti-6Al-4V alloy,” J. Mater. Sci. Technol., vol. 34, no. 5, pp. 782–787, May 2018, doi: 10.1016/j.jmst.2017.07.016.

[46] A. Sharma, M. C. Oh, J.-T. Kim, A. K. Srivastava, and B. Ahn, “Investigation of electrochemical corrosion behavior of additive manufactured Ti–6Al–4V alloy for medical implants in different electrolytes,” J. Alloys Compd., vol. 830, p. 154620, Jul. 2020, doi: 10.1016/j.jallcom.2020.154620.

[47] A. Cigada, M. Cabrini, and P. Pedeferri, “Increasing of the corrosion resistance of the Ti6Al4V alloy by high thickness anodic oxidation,” J. Mater. Sci. Mater. Med., vol. 3, no. 6, pp. 408–412, Nov. 1992, doi: 10.1007/BF00701236.

[48] P. Metalnikov, G. Ben-Hamu, and D. Eliezer, “Corrosion behavior of AM-Ti-6Al-4V: a comparison between EBM and SLM,” Prog. Addit. Manuf., vol. 7, no. 3, pp. 509–520, Jun. 2022, doi: 10.1007/s40964-022-00293-8.

[49] J. Fojt et al., “Corrosion behaviour and cell interaction of Ti-6Al-4V alloy prepared by two techniques of 3D printing,” Mater. Sci. Eng. C, vol. 93, pp. 911–920, Dec. 2018, doi: 10.1016/j.msec.2018.08.066.

[50] H. Zhang et al., “Different corrosion behaviors between α and β phases of Ti6Al4V in fluoride-containing solutions: Influence of alloying element Al,” Corros. Sci., vol. 169, p. 108605, Jun. 2020, doi: 10.1016/j.corsci.2020.108605.

[51] C. Örnek, C. Leygraf, and J. Pan, “On the Volta potential measured by SKPFM – fundamental and practical aspects with relevance to corrosion science,” Corros. Eng. Sci. Technol., vol. 54, no. 3, pp. 185–198, May 2019, doi: 10.1080/1478422X.2019.1583436.